Hindawi
Advances in Civil Engineering
Volume 2024, Article ID 6929522, 13 pages
https://doi.org/10.1155/2024/6929522

Research Article

Mechanical Performance of Tube-Gusset X-Joints Enhanced by Ring Plates

Xiaolu Li,[1] Zhe Yang,[1] Yan Zhao,[1] Xinwu Wang,[1] Xiaomin Xue,[2] and Xueming Wang[3]

[1]*School of Civil Engineering, Luoyang Institute of Science and Technology, Luoyang, China*
[2]*Department of Civil Engineering, Xi'an Jiaotong University, Xi'an, China*
[3]*China Power Engineering Consulting Group, Xi'an, China*

Correspondence should be addressed to Zhe Yang; 200902201801@lit.edu.cn

Received 6 December 2023; Revised 24 February 2024; Accepted 20 March 2024; Published 4 April 2024

Academic Editor: Tafsir Tafsirojjaman

This study aims to investigate the effect of the ring plate on the mechanical performance of X-type tube-gusset joints. The failure modes, ultimate strengths, and failure mechanisms of X-joints with ring plates were investigated through experiments and finite element analyses. The results indicated that the ring plate and the chord within the effective range of the ring plate constituted the primary bearing structure of the X-joint. Increases in the ring plate thickness and width increased the ultimate strength of the X-joint. By considering the forces of the braces as a superposition of the bending moment and the force acting on the gusset of the X-joint, a simplified calculation method for the ultimate strength of X-joints was established. The derivation process was validated and refined through experiments and finite element analyses. Finally, a safe and reliable formula was derived for evaluating the ultimate strength of X-joints.

1. Introduction

Tubular steel towers have become increasingly prevalent in ultra-high voltage transmission lines owing to their exceptional mechanical properties and architectural appeal. The joints in a tubular steel tower are created by the convergence of members within the tower, making the study of the mechanical properties and failure modes of these joints crucial for the design of these towers [1]. Two types of joints are commonly used in tubular towers: tubular and tube-gusset [2]. In the tubular joint, each diagonal member is directly welded to a chord; this underlines the precise processing and high-quality welding. Therefore, the application of tubular joints is limited because tubular steel towers are primarily deployed in harsh and remote environments. Accordingly, this has led to the development of tube-gusset joints that are argued to be more suitable for constructing transmission towers. The tube-gusset joint comprises gussets, bolts, chords, and brace members. The gusset is welded to the chord wall, and bolts connect the brace members to the gusset. In addition, ring plates are commonly used in tube-gusset joints to enhance their mechanical properties [3, 4]. However, no prominent design guide is available for the ring plate; thus, the dimensions of the annular plate are primarily determined based on experience [5]. Therefore, this study evaluated the ultimate strength of tube-gusset joints with ring plates.

The exploration of tube-gusset joints was initiated by Japanese scholars in 1974 [6], and various standards have since been established for designing tube-gusset joints, including those proposed by IIW [7], CIDECT [8], KBC [9], and AISC [10]. To date, several techniques have been used to strengthen the chord wall [11, 12]. Nassiraei [13, 14] discussed the effect of collar plates on the static capacity and local joint flexibility of circular hollow section X-joints through experimental and numerical investigations. They noted that the collar plates made the deformation of the reinforced joints in the near joint intersection more uniform than that of the unreinforced joints. Therefore, the collar plate could significantly increase the static strength of the joints. In addition, the collar plate size could affect the ultimate strength of joints [15]. A theoretical formula was also proposed based on the yield body theory. In addition, research has shown that fiber-reinforced polymers can improve the static capacity of tubular X-joints [16]. Similarly, ring plates are effective in reinforcing tube-gusset joints. Furthermore, the

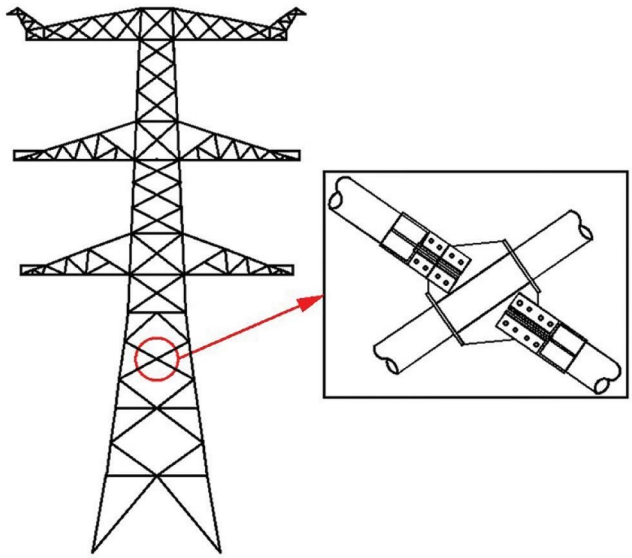

Figure 1: Sketch of X-joints.

introduction of ring plates notably influences the performance of the tube-gusset joints. The Japanese Steel Tubular Association proposed a formula for designing tube-gusset joints stiffened by annular plates [17]; however, these formulae are deemed overly complex for practical engineering applications. Moreover, the empirical evidence suggests that the results obtained from these formulae tend to be overly conservative [17, 18].

Recently, the application of ring plates in joint designs has attracted increasing attention. Li and Deng [19, 20] delved into the ultimate bearing capacities of planar K- and multi-planar DK-joints through experimental and numerical investigations, revealing a "push–pull" deformation mechanism in both the K and DK joints. Li et al. [21, 22] explored the impact of ring plates on the ultimate strengths of KT- and X-joints. Qu and Sun [23–28] conducted a comprehensive examination of the mechanical performance of KT joints and highlighted the inapplicability of the formulae designed for low-strength steel in the context of high-strength steel joints. Comparisons between the mechanical properties of the KK-type and K-type joints were also presented [29]. Sitong et al. [30] investigated an analytical model for the load distribution in multiple-ring-stiffened tube-gusset joints, whereas Chen et al. [31] studied the application of ring plates in tubular joints. In general, 1/4 ring plates are primarily used in K-type or KK-type joints, and full-ring plates are generally used in X-type joints. Gaps still exist in the understanding of the impact of ring plates on the load-bearing performance of tube-gusset joints.

This study focussed on examining the mechanical behavior of X-type tube-gusset joints with ring plates, as shown in Figure 1. By analyzing the forces acting on the X-joints and considering the joint under the action of the braces as a superposition of the bending moment (M) and force (P), the ring plate and the chord within the effective range of the ring plate were regarded as the primary bearing structures of the X-joint. A simplified calculation method for the ultimate strength of an X-joint was proposed. To optimize this method, specimens with a 90° angle between the brace and the chord were selected, corresponding precisely to the condition of the force (P) on both sides of the chord. Concurrently, finite element analysis was performed on the X-joint, and the results were compared with the experimental results. Subsequently, a parameter analysis was performed using the validated finite element model. The failure mode and ultimate strength of the X-joints under force and bending moment were investigated, and the main factors influencing the ultimate strength of the X-joints were discussed. Finally, a suitable formula for the ultimate strength of X-joints was proposed and demonstrated to be safe and reliable. This contribution is invaluable for designing X-joints with ring plates.

2. Force Analysis of the Tube-Gusset Joint

2.1. Calculations for JSSC. Because of the influence of the ring plate, the primary resistance of the joint lies in the ring plate and its accessories. According to Japanese Society of Steel Construction (JSSC) [17], the forces exerted by the braces are converted into a force that acts directly on the ring plate. As shown in Figure 2, the force on the brace (F) is transformed into the bending moment (M) and tensile (or compression) force (P) acting on the root center of the gusset plate.

$$P = F \sin \theta, \tag{1}$$

$$M = F \cos \theta \cdot \frac{D}{2}, \tag{2}$$

$$Q = F \cos \theta. \tag{3}$$

Subsequently, these forces are further converted to the positions of the ring plates as follows:

$$P_{V1} = \frac{M}{B} + \frac{P}{2}, \tag{4}$$

$$P_{V2} = \frac{M}{B} - \frac{P}{2}, \tag{5}$$

$$P_V = \max (P_{V1}, P_{V2}). \tag{6}$$

Table 1 presents the computational formula proposed by JSSC for tube-gusset joints with ring plates.

2.2. Analytical Model. As indicated in Table 1, the calculation process is complex for designers, and the formula results exhibit a conservative bias. In this study, we aimed to derive a more straightforward and reliable calculation formula.

According to Equations (1)–(3), the force on the brace (F) is transformed into the bending moment (M), tensile (or compression) force (P), and shear force (Q). The consideration of punching shear is omitted because of the large axial compression ratios of the chords in transmission towers [14]. Consequently, as illustrated in Figure 2(a), the joint under the influence of the braces is viewed as a superposition of the bending moment (M) and force (P).

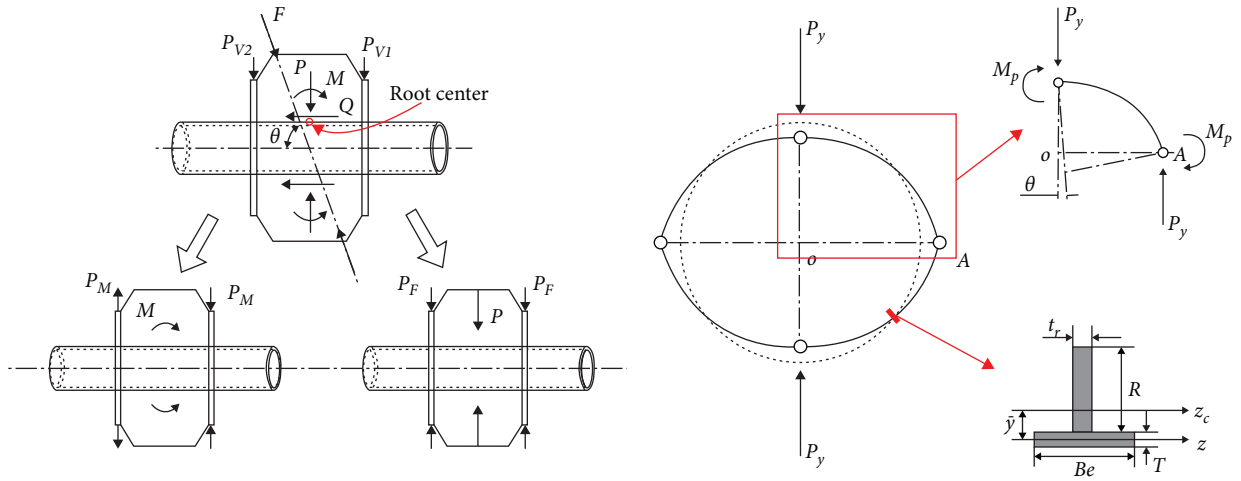

FIGURE 2: Resistance mechanism of the X-joint: (a) simplification of force; (b) resistance mechanism of the X-joint.

TABLE 1: Computing formula proposed by JSSC.

	Computing formula	
1	$P_{y1} = 2(BeT + Rt_r)\sigma_{Br}X$	
	$f < \frac{1}{8}(8 + \frac{D}{R} - \sqrt{(\frac{D}{R})^2 + 32})$	$(1 + 2f - f^2) - 2(1 + f)^2X^2 = (1 + f)(\frac{D}{R} + 1 - f)X$
	$1 > f \geqslant \frac{1}{8}(8 + \frac{D}{R} - \sqrt{(\frac{D}{R})^2 + 32})$	$3 - f - (1 + \sqrt{3})(1 - f)X - 2(1 + f)X^2 = 2(1 + f)(\frac{D}{R} + 1 - f)X$
	$\frac{2R}{D} + 1 > f > 1$	$3 - f - (1 + \sqrt{3})(1 - f)X - 2(1 + f)X^2 = \frac{2D}{R}X$
	$f \geqslant \frac{2R}{D} + 1$	$X = \frac{2R}{D(1+f)}$
2	$P_{y2} = \frac{2Rt_r\sigma_{yr}}{\sqrt{3}}$	
3	$P_y = \min(P_{y1}, P_{y2})$	

In which, $Be = 1.07\sqrt{T(D - T)} + t_r$, $f = \frac{BeT}{Rt_r}$.

$$P_M = \frac{M}{B}, \tag{7}$$

$$P_F = \frac{P}{2}. \tag{8}$$

Next, the resistance mechanism of the X-joint is simplified to a circular ring with a T-shaped cross-section, where *Be* represents the effective range of the ring plate, as shown in Figure 2(b). The load on the X-joint can be reasonably equated to that on the ring plate adhering to the following equilibrium conditions.

$$\frac{2M_P}{P_y} = \frac{\sqrt{2}}{2}r_p \cos\left(\frac{\pi}{4} - \theta\right), \tag{9}$$

where M_p denotes the cross-sectional plastic moment, and r_p denotes the radius of the ring. The failure load of the structure can be determined according to the principles of virtual work as follows:

$$P_y = \frac{4M_P}{r_P}. \tag{10}$$

In accordance with Chinese standard DL/T5085-1990 (1999), the effective range of the ring plate is defined as follows:

$$\mathrm{Be} = (0.63 + 0.88R/D)\sqrt{DT} + t_r. \tag{11}$$

Assuming $f = \frac{\mathrm{BeT}}{Rt_r}$, the value of f is <1 for R within the range $0.25 \leq R/D \leq 0.75$. Thus, the neutral axis of the cross-section can be expressed as follows:

$$\overline{y} = \frac{R + T}{2(1 + f)}. \tag{12}$$

The radius of the ring, r_p, can be expressed as follows:

$$r_P = \left(\frac{D - T}{2} + \overline{y}\right). \tag{13}$$

The cross-section plastic moment of the ring can be expressed as follows:

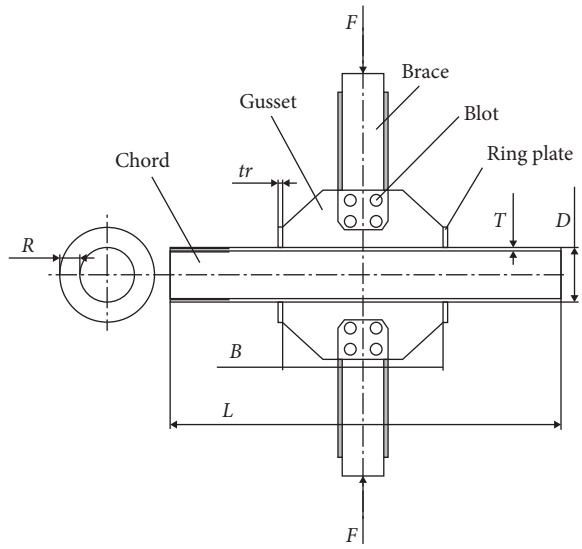

Figure 3: Schematic of the specimen.

$$M_P = \sigma_y t_r \left(R + \frac{T}{2} - \overline{y} \right)^2. \tag{14}$$

Substituting into Equation (10), the failure load of the X-joint can be obtained as follows:

$$P_y = \frac{4\sigma_y t_r \left(R + \frac{T}{2} - \overline{y} \right)^2}{(D - T)/2 + \overline{y}}. \tag{15}$$

3. Test Program and Finite Element Analysis

3.1. Specimens and Loading. Considering the test conditions, specimens with a 90° angle between the brace and the chord were selected. This configuration corresponds precisely to the force condition (P) on both sides of the chord, as illustrated in Figure 2. Figure 3 shows a schematic of the specimen. Seven specimens were examined; their main geometric dimensions are listed in Table 2. Notably, because of limitations in the sample size, the experiment primarily focused on investigating the effect of the ring plate on the ultimate strength of the joints. Table 2 presents the adoption of three types of steel tubes ($\Phi 194 \times 6$, $\Phi 273 \times 6$, and $\Phi 356 \times 8$) for the chord members. Additionally, to mitigate the end condition effect in the tests [32], the chord length (L) was set to 2,000 mm. To prevent overall buckling, the selected brace members were fashioned from $\Phi 159 \times 6$ steel tubes with a length of 500 mm. The width (H) and thickness (t_g) of the gusset plate were 300 and 16 mm, respectively.

Furthermore, the ring plates were prepared from Q235 steel, and Q345 steel was used for the remaining parts of the specimens. Tensile tests were conducted to assess the mechanical performances of the steel materials, and the results are listed in Table 3.

The test setup is shown in Figure 4. The specimen was horizontally positioned in the loading frame. Both ends of the chord were welded to the endplate, with bolts securing the chord ends to the loading frame. Hydraulic machines were used to load the brace members with an axial force.

Table 2: Dimensions of the specimens.

Specimen	Dimensions (mm)					
	D	T	R	t_r	B	t_g
$\Phi 194 \times 6 - 6 \times 80$	194.0	6.26	5.55	81.71	650	16
$\Phi 194 \times 6 - 10 \times 80$	194.1	6.29	9.92	81.70	650	16
$\Phi 194 \times 6 - 10 \times 100$	194.1	6.36	9.29	102.44	650	16
$\Phi 273 \times 6 - 6 \times 48$	273.0	6.06	5.61	48.54	650	16
$\Phi 273 \times 6 - 6 \times 72$	273.0	5.93	5.56	71.92	650	16
$\Phi 356 \times 8 - 8 \times 48$	356.0	8.55	7.95	49.15	650	16
$\Phi 356 \times 8 - 8 \times 120$	356.1	8.03	7.72	120.44	650	16

To eliminate potential gaps between the specimens and the hydraulic machine, a preloaded force of approximately 1–2 kN was applied to each brace member before the test. During the test, the two brace members were progressively loaded in a 1 : 1 ratio until the joint collapsed.

Four linear variable differential transformers (LVDTs) were used in the tests (Figure 4). LVDT1 and LVDT2 were positioned at the two sides of the chord near the left ring plate, whereas LVDT3 and LVDT4 were situated near the right ring plate. Strain gauges were strategically placed on both the chord and ring plate. Given the symmetrical structure of the X-joint, the strain gauges were arranged on only one side of the joint, as shown in Figure 4(b). Strain gauges on the chord were spaced 30° apart at the section near the ring plate, whereas those on the ring plate were positioned at 0° and ±90°.

3.2. FE Analytical Method. General nonlinear finite element software ANSYS was employed for the numerical analysis of the X-joints. The eight-node shell element (shell281) was used. The specimen material was simulated using an isotropic hardening model based on the Von Mises yield criterion. The stress–strain curves derived from the tensile tests were incorporated into the finite element (FE) models. By employing a time-stepping nonlinear analysis with a large allowance for deformation and a Newton–Raphson method equation solver, the FE models of the X-joints are illustrated in Figure 5(a). As shown in Figure 5(a), no bolt model was established; instead, coupling around the bolt holes was achieved using MPC184. Similarly, each end of the chord and brace members was coupled with MPC184 to facilitate the load application. Compared with fatigue analysis, the influence of welds on the accuracy of static analysis is relatively small [2, 33, 34]. Qu et al. [26] and Sitong et al. [30] used the shell281 element to model the tube-gusset joints in their research but did not establish a weld model. The accuracy of the FE model was evaluated by comparing its results with the test results, including the failure mode, strain–load relationship, and load–displacement curve. The FE model matched well with the experimental results. Sitong et al. [30] proved that the proposed analytical model could accurately predict the distributed load of every ring stiffener at the tube-gusset joint with errors never exceeding 5%. In the

Table 3: Material properties of the specimens.

Component	Type	Yield stress (MPa)	Tensile strength (MPa)	Poisson's ratio	Elastic modulus (MPa)
Chord	$\Phi 194 \times 6$	441.44	492.92	197.82	0.215
	$\Phi 273 \times 6$	405.57	513.69	165.04	0.228
	$\Phi 356 \times 8$	405.57	513.69	165.04	0.228
Ring plate	$t_r = 6$	334.66	483.21	188.77	0.395
	$t_r = 8$	291.72	421.33	179.62	0.394
	$t_r = 10$	315.18	455.81	202.51	0.393

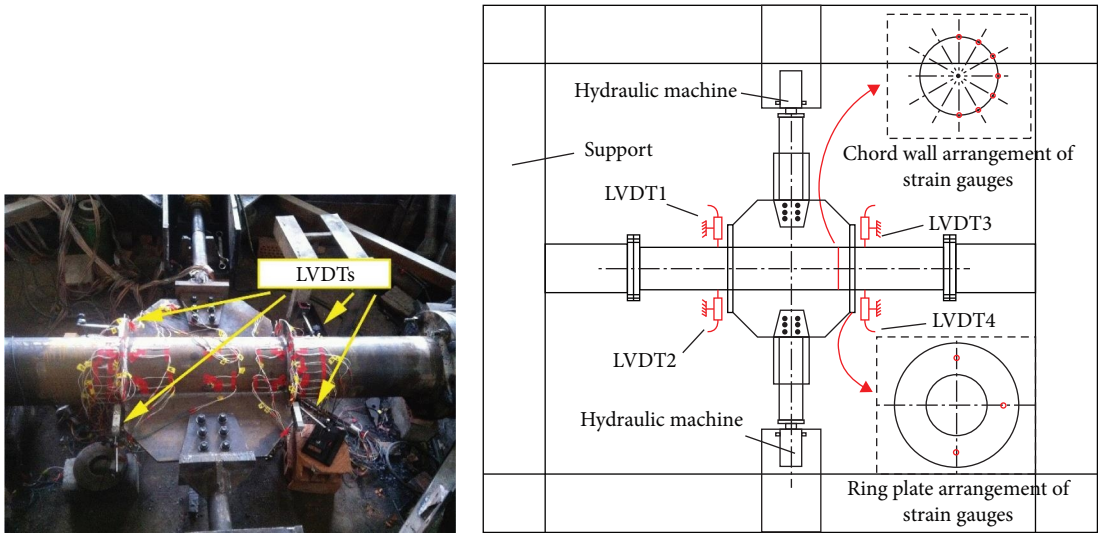

Figure 4: Experimental setup: (a) experimental setup of $\Phi 273 \times 6 - 6 \times 72$; (b) schematic of the experimental setup.

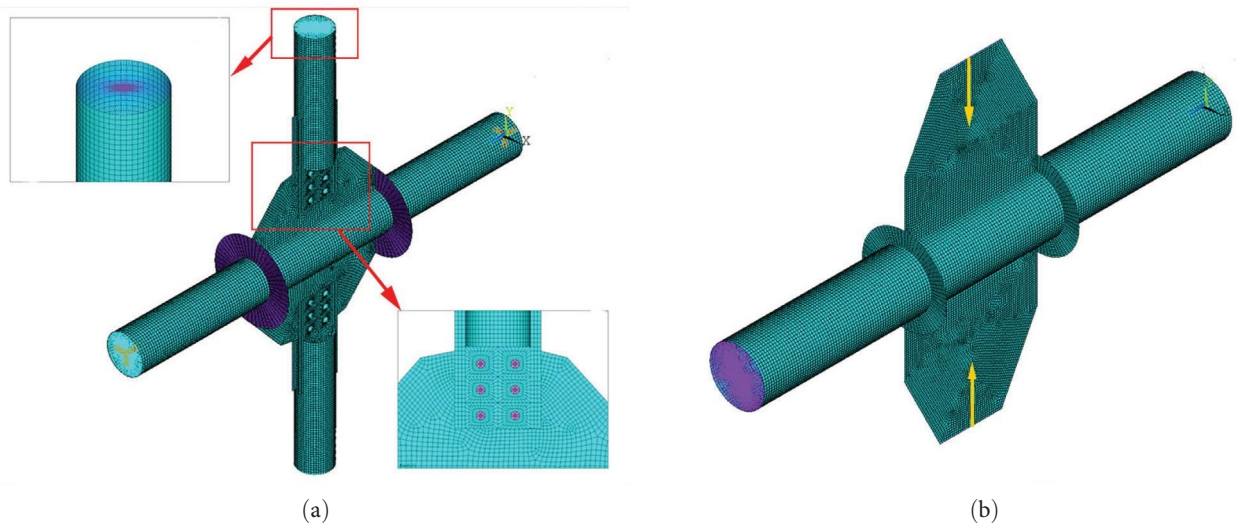

Figure 5: FE models of the specimen: (a) test model of the X-joint; (b) equivalent model of the X-joint.

present study, the failure mode of the X-joint was caused by chord depression and ring-plate deformation. The strain and deformation results were obtained around the chord surface weld. Therefore, the weld was not modeled in this study.

In line with the observations by Vegte and Makino [32], the strength of the joint was assumed to be significantly influenced by the boundary conditions. However, this effect was only notable for brace tension cases with low brace

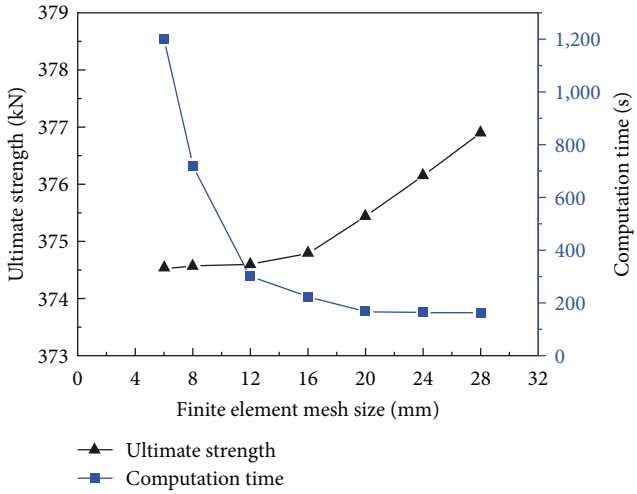

Figure 6: Mesh sensitivity analysis.

angles [35]. Consequently, this study adopted a fixed boundary condition for the chord. The two ends of the braces were restrained except for the axial displacement. Figure 5(b) shows the equivalent model of the X-joints, where the brace forces were substituted by a force on the gusset plate.

A preliminary finite element analysis was performed to examine the influence of the mesh size on the ultimate strength of the X-joint. As shown in Figure 6, the gained ultimate strength increased, and the computing time decreased when the finite element mesh size increased. The ultimate strength did not significantly differ within a mesh size of <12 mm. However, a further reduction in the mesh size would significantly increase the computing time. Thus, a nominal element size of 12 mm was selected for the FE model to ensure accuracy and efficiency.

4. Discussion

4.1. Verification of the FE Analysis. Given that the gusset plate, braces, and welds remained undamaged throughout the tests, this study did not explore punching shear failure. The numerically determined load-deformation curves, along with the dotted lines representing the tests, are plotted in Figure 7. The predominant failure modes occurred in the chord wall and ring plates, as shown in Figure 8. A significant correlation was observed between the experimental and numerical analysis results for the failure modes. Table 4 outlines the ultimate strength derived from the FE analysis, demonstrating a mean error of 3.8% with a corresponding standard deviation of 0.035. Table 4 lists the calculation results for the three specimens without ring plates. Notably, the setting of the ring plates could significantly improve the ultimate strength of the tube-gusset joint. The strain results at the critical points, as illustrated in Figure 9, confirmed that the FE model accurately reflected the strain state of the X-joints.

Considering Figures 7–9 and Table 4, in conclusion, the FE model successfully predicted the structural performance and strength of the X-joints. Figure 10 further confirms the matching between the equivalent model and the FE models with braces, validating their use in subsequent studies.

4.2. Failure Mode of X-Joints. As shown in Figure 7, during the initial loading period, the chord deformation increased linearly with load. As the load continued to increase, a turning point appeared in the load–displacement curve. At last, the chord displacement rapidly increased, and eventually, the joint failed. A similar trend was observed in the variation of the strain values at the measurement points. As shown in Figure 9(b), the strain increased linearly when the load was less than 200 kN. As the load continued to increase, the increased rate of strain gradually accelerated. A turning point appeared on the curve. After the load reached 450 kN, the load did not increase significantly; however, the strain rapidly increased. This indicated that the joint had already failed.

Figure 11 illustrates the stress nephograms of $\Phi 273 \times 6 - 6 \times 72$ under forces of 216 and 250 kN. Combining Figure 9(a), the failure process of the X-joints could be analyzed as follows: in the initial loading phase, the strain values at the chord wall were within 0.001. This indicated that the chord wall deformation was in the elastic range. As the load increased, the chord deformation continued to increase. When $F = 360$ kN, the strain values at positions 0°, 90°, 180°, and −90° on the chord were close to 0.001. When the loading continued, at $F = 460$ kN, the strain values at these four positions were significantly higher than those at the other positions. This indicated that four plastic hinges appeared at positions 0°, 90°, 180°, and −90° on the chord.

Figure 12 illustrates stress nephograms of $\Phi 273 \times 6 - 6 \times 72$ under a bending moment. Deformation of the chord and warping of ring plates were observed. During the elastic stage, the stress on the chord was relatively high only at the position near the ring plate, whereas the stress at other positions was minimal. In the final state, one side of the chord was concave, whereas the other side was elongated, resulting in an elliptical deformation of the ring plates near the chord (Figure 12(b)).

The failure mode suggested that the ring plate and the chord within the effective range of the ring plate constituted the main bearing structure of the X-joint, thereby validating the theoretical derivation in Section 2.

4.3. Comparison between Force and Bending Moment on Gusset Plates. Under the bending moment, one side of the chord was concave, whereas the other side was elongated. Considering the absolute value of the chord deformation as the horizontal coordinate would produce the load–deformation curve, as shown in Figure 13. The deformation trends at the two locations were essentially identical. During the initial loading period, the deformation increased linearly with the load, indicating an elastic stage. When the deformation exceeded 2 mm, the chord deformed rapidly until the joint failed. However, the deformation at the chord compression point was slightly greater than that at the tension point. For design safety considerations, the ultimate strength of the joint was determined based on the location with more substantial deformation, that is, the compression point.

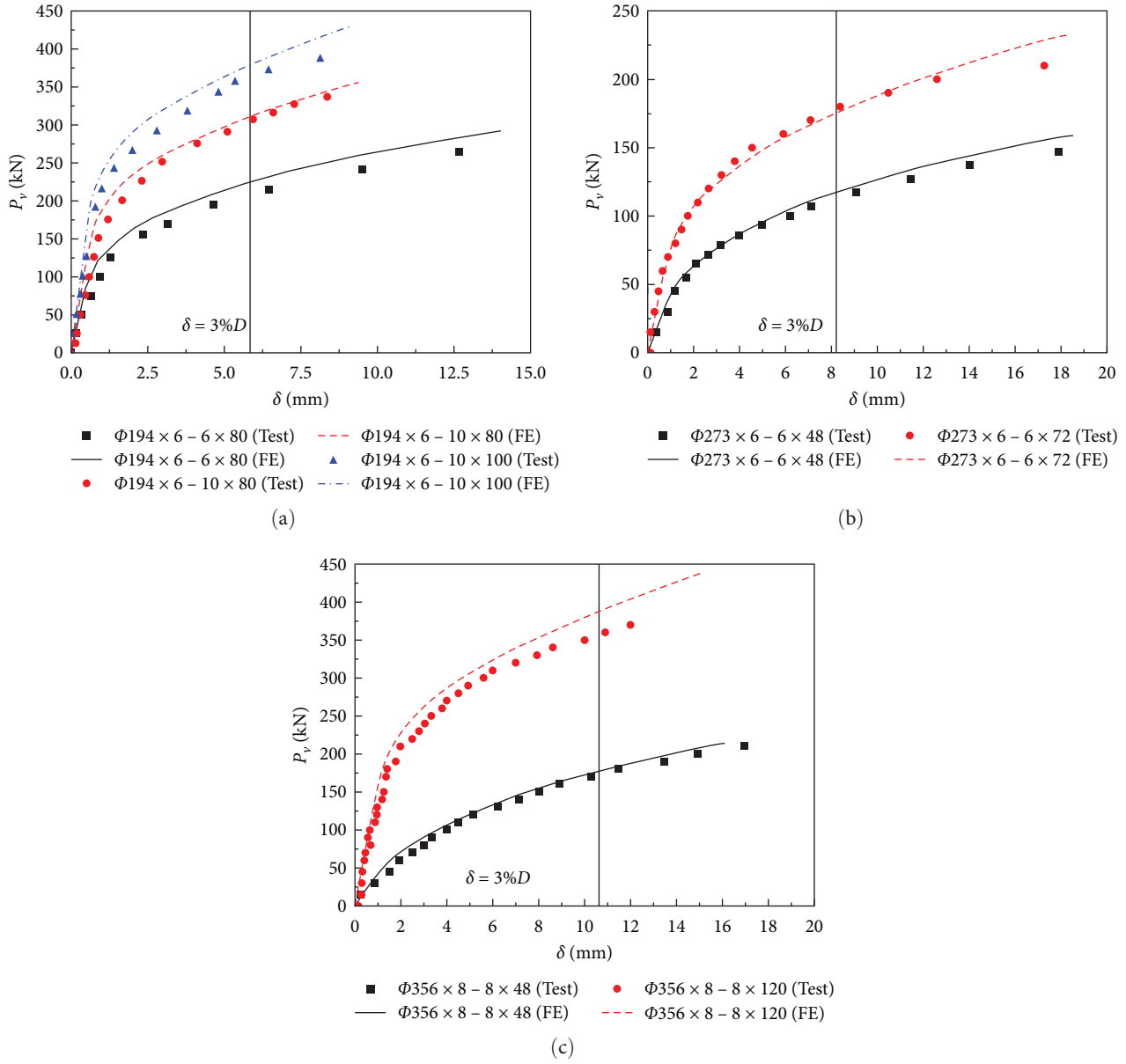

Figure 7: Load–displacement curves: (a) $D = 194$ mm; (b) $D = 273$ mm; (c) $D = 356$ mm.

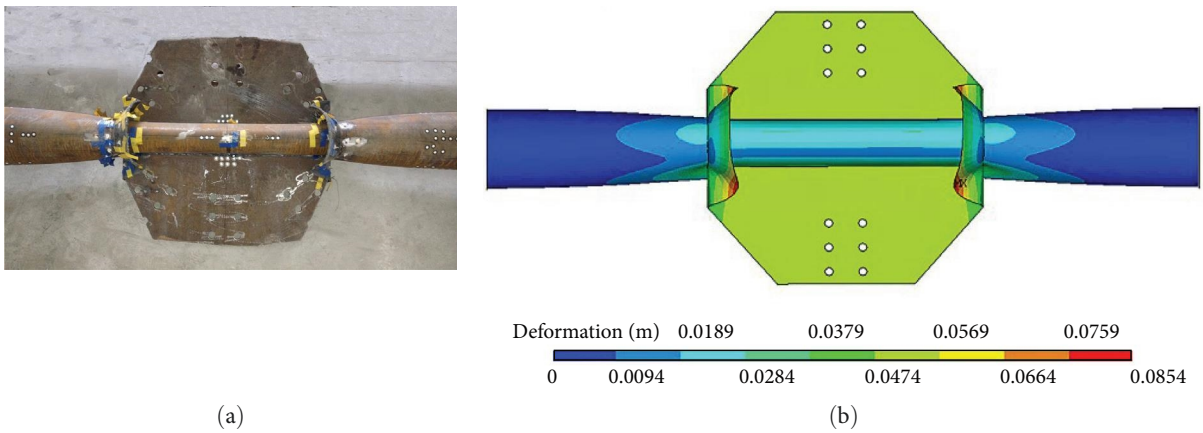

Figure 8: Failure mode of $\Phi 194 \times 6 - 10 \times 100$: (a) test; (b) FE analysis.

Table 4: Ultimate strengths gained from tests and FE analysis.

Specimen	Ultimate strength (kN)		
	$P_{y\text{-Test}}$	$P_{y\text{-FE}}$	$(P_{y\text{-FE}} - P_{y\text{-Test}})/P_{y\text{-Test}} \times 100\%$
$\Phi 194 \times 6 - 0 \times 0$	—	72.09	—
$\Phi 194 \times 6 - 6 \times 80$	208.78	224.42	7.5%
$\Phi 194 \times 6 - 10 \times 80$	305.03	310.67	1.8%
$\Phi 194 \times 6 - 10 \times 100$	365.13	378.50	3.7%
$\Phi 273 \times 6 - 0 \times 0$	—	55.24	—
$\Phi 273 \times 6 - 6 \times 48$	113.11	117.37	3.8%
$\Phi 273 \times 6 - 6 \times 72$	178.81	175.47	−1.9%
$\Phi 356 \times 8 - 0 \times 0$	—	88.54	—
$\Phi 356 \times 8 - 8 \times 48$	173.15	178.24	2.9%
$\Phi 356 \times 8 - 8 \times 120$	357.30	388.40	8.7%
Average	—	—	3.8%
Standard deviation	—	—	0.035

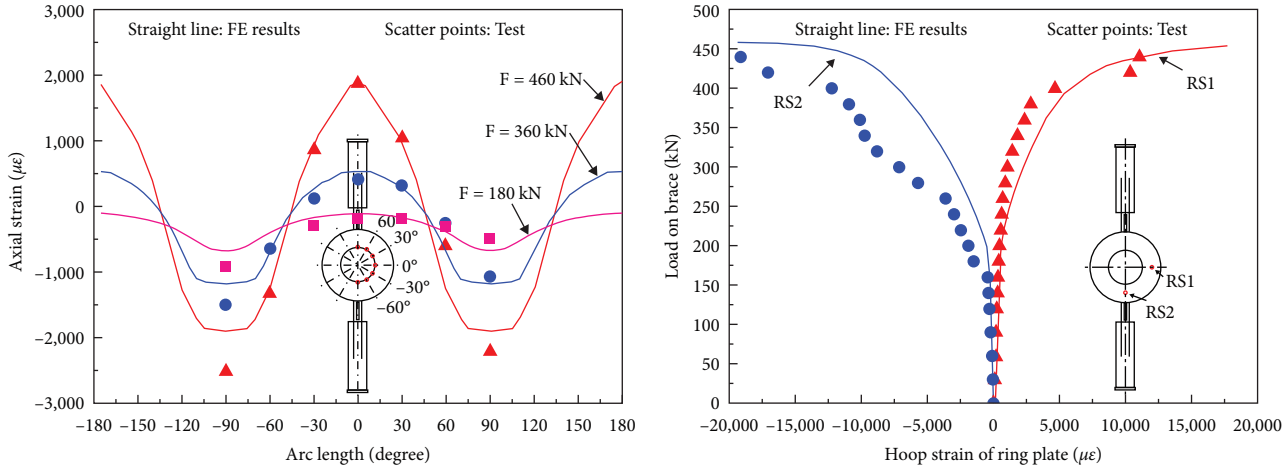

(a) (b)

Figure 9: Strain results of $\Phi 273 \times 6 - 6 \times 72$ (strain gauges location in Figure 4): (a) axial strain along the circumference; (b) strain at key points.

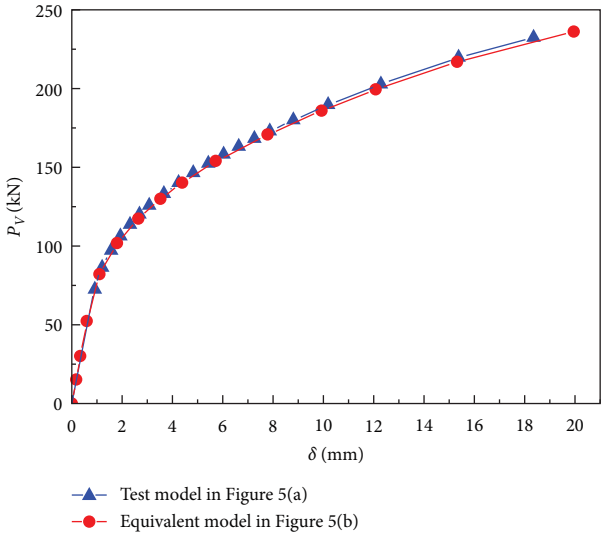

Figure 10: Validation of FE models.

Figure 14 shows a comparison between the ultimate strengths of the X-joints under force and bending moment, revealing extremely close values with a mean ratio of 0.9767 and a standard deviation of 0.0365. This confirmed the reasonableness of the calculation method in Equations (1)–(3).

5. Parameter Analysis

In this section, the verified simulation model is used to discuss the mechanical properties of the X-joint under an axial force. To enhance the calculation efficiency, the X-joint model was simplified by eliminating brace member deformations and applying forces directly to the gusset plates.

The results indicated that an increase in the thickness and width of the ring plate improved the ultimate strength of the X-joints. Two dimensionless parameters, namely, the ring plate thickness-to-chord ratio (t_r/T) and the width of the ring plate to the chord diameter ratio (R/D), were considered. Following the Code for Design of Steel–Concrete Composite

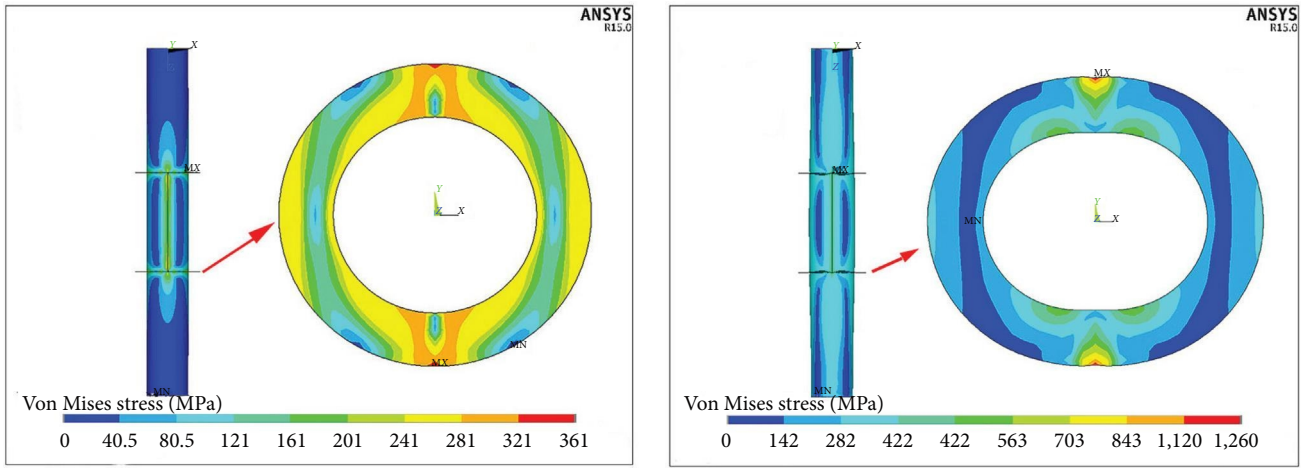

(a) (b)

Figure 11: Stress nephograms of $\Phi 273 \times 6 - 6 \times 72$ under force: (a) $F = 216$ kN; (b) $F = 462$ kN.

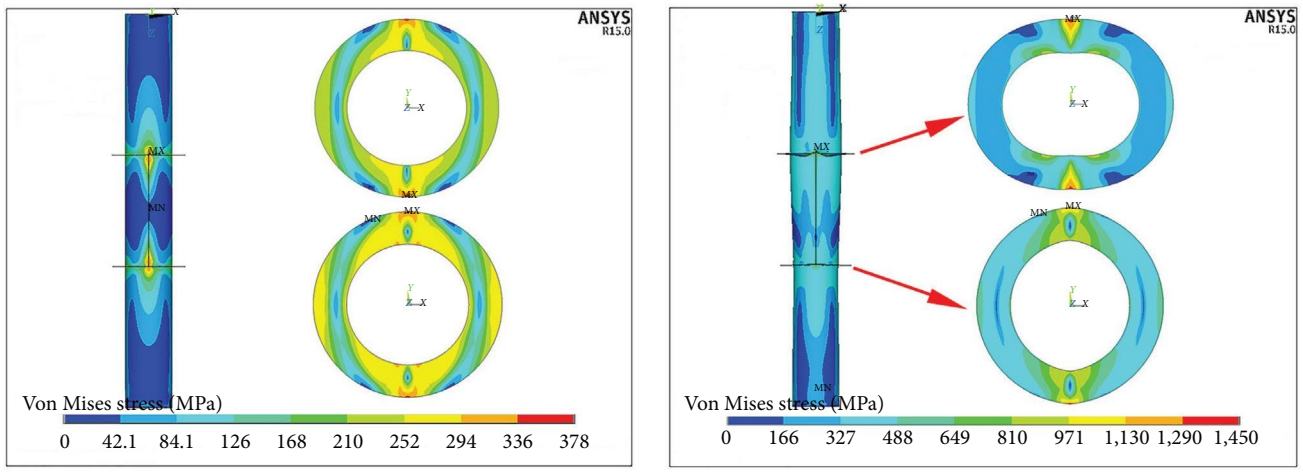

(a) (b)

Figure 12: Stress nephograms of $\Phi 273 \times 6 - 6 \times 72$ under bending moment: (a) $M = 78$ kN m; (b) $M = 169$ kN m.

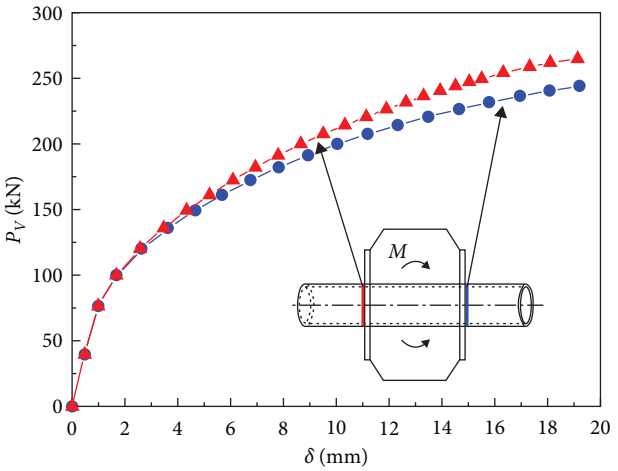

Figure 13: Deformation of the bending moment.

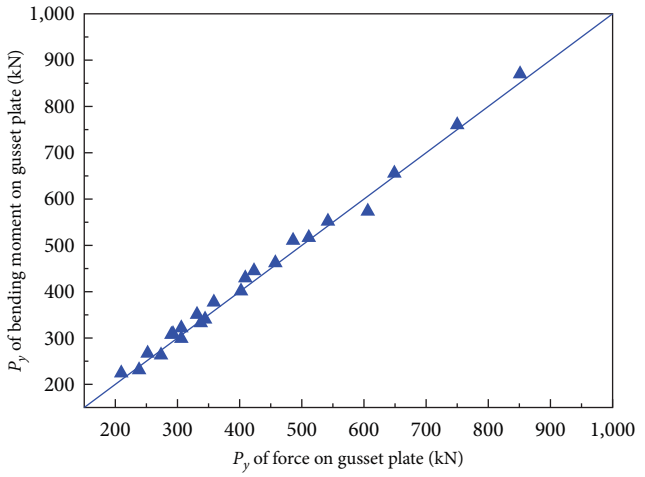

Figure 14: Ultimate strength of the X-joints.

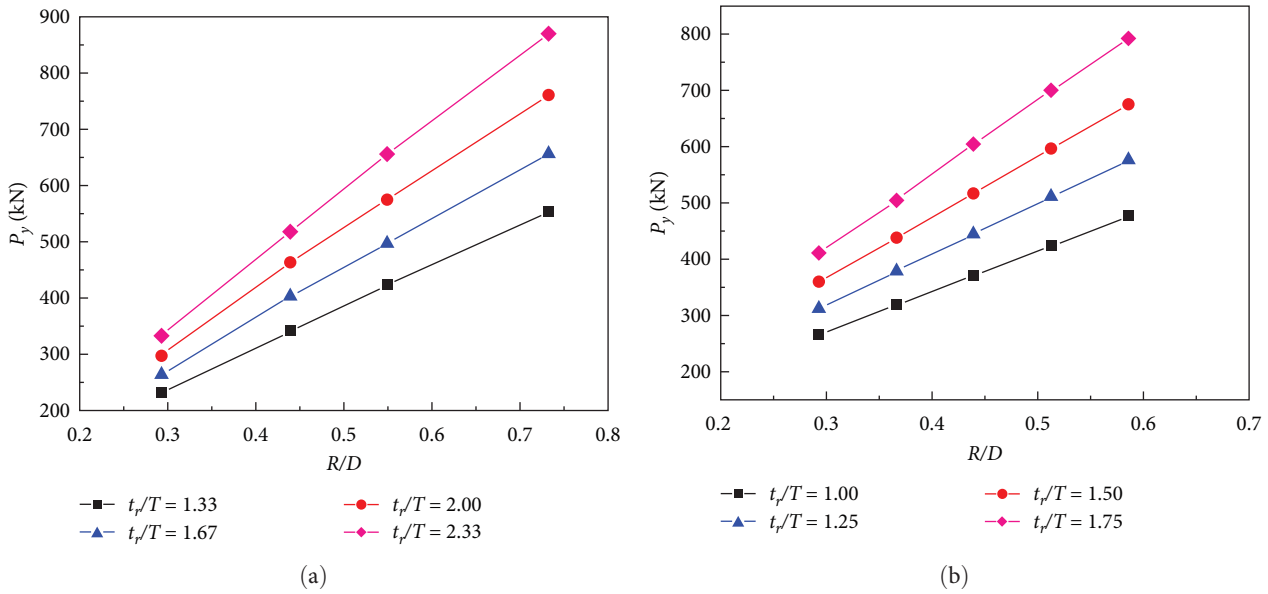

Figure 15: Effects of R/D on the ultimate strength of the X-joints under lateral pressure: (a) $D = 273$ mm and $T = 6$ mm; (b) $D = 273$ mm and $T = 8$ mm.

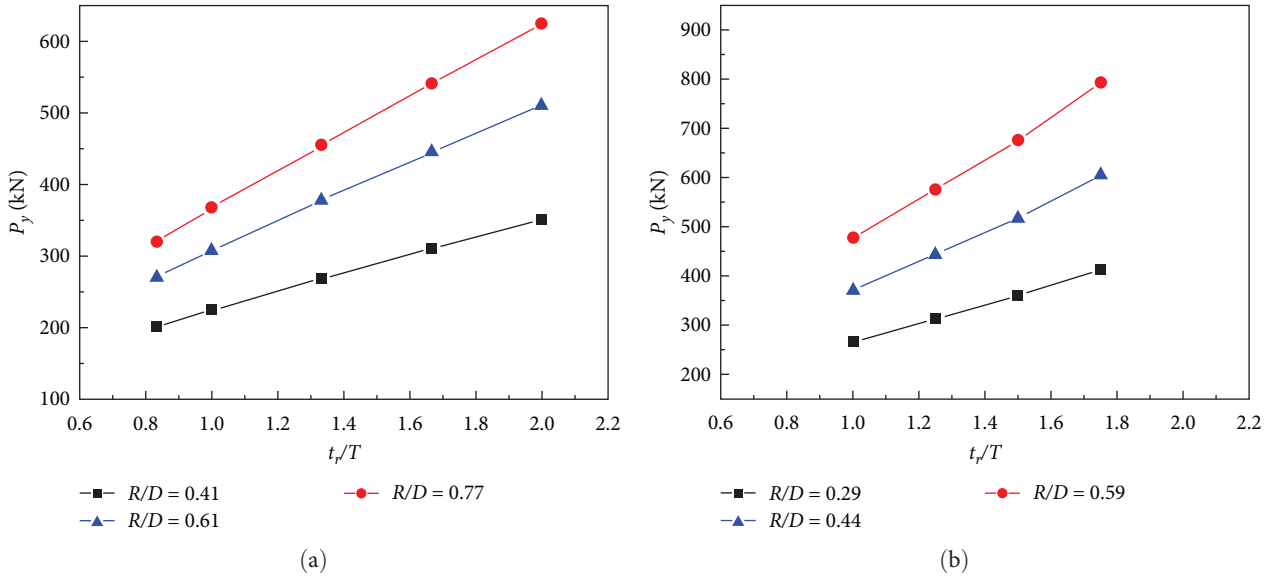

Figure 16: Effects of t_r/T on the ultimate strength of the X-joints under lateral pressure: (a) $D = 194$ mm and $T = 6$ mm; (b) $D = 273$ mm and $T = 8$ mm.

Structure in China (1999), parametric study parameters were set at $0.25 \leq R/D \leq 0.75$ and $219\text{ mm} \leq D \leq 426\text{ mm}$.

Figures 15 and 16 show the effects of t_r/T and R/D, respectively, on the ultimate strengths of the X-joints under an axial force. As shown in Figure 15, as R/D increased, the ultimate strength of the joint increased in a near-linear manner. Similarly, a near-linear relationship was observed between the ultimate strength of the X-joints and the value of t_r/T, as shown in Figure 16. Therefore, the joint strength was inferred to be increased by the ring plates.

Figure 17 shows the effect of D/T on the ultimate strength of X-joints with $R = 80$ mm and $t_r = 8$ mm. An increase in the value of D/T resulted in a decrease in the ultimate strength of the X-joints. However, the ultimate strength changed only slightly when $D/T > 60$. Because changes in D/T significantly affected the weight of the X-joints, the impact caused by D/T was not as significant as those caused by R/D and t_r/T.

6. Recommended Formulae for the Ultimate Strength of the X-Joint

6.1. Revised Formula for the Ultimate Strength of the X-Joint. In Section 2.2, the resistance mechanism of the X-joint is simplified to a circular ring with a T-shaped cross-section. When the X-joint fails, four plastic hinges appear at positions

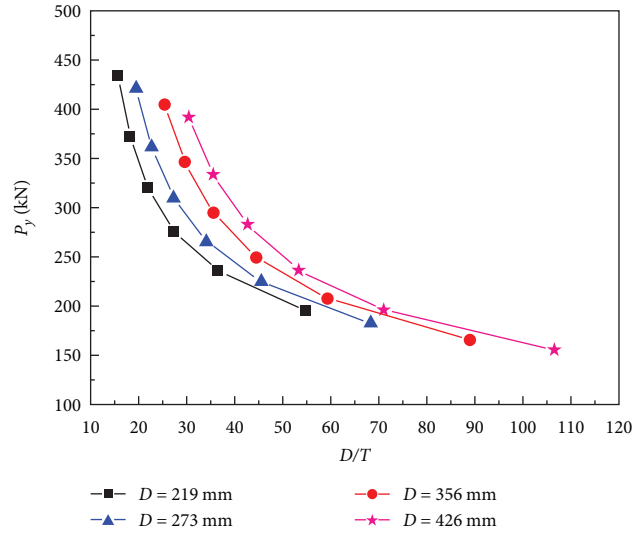

Figure 17: Effects of D/T on the ultimate strength of the X-joints under lateral pressure ($R = 80$ mm and $t_r = 8$ mm).

Table 5: Ultimate strength of the specimens.

Specimen	Ultimate strength (kN)				Error: $(P_y - P_{y\text{-Test}})/P_{y\text{-Test}} \times 100\%$)		
	$P_{y\text{-Test}}$	$P_{y\text{-JSSC}}$	P_{y-1}	P_{y-2}	e_{JSSC}	e_1	e_2
$\Phi 194 \times 6 - 6 \times 80$	208.78	130.25	198.99	203.83	−37.6%	−4.7%	−2.37%
$\Phi 194 \times 6 - 10 \times 80$	305.03	217.08	280.14	287.84	−28.8%	−8.2%	−5.63%
$\Phi 194 \times 6 - 10 \times 100$	365.13	271.35	387.55	359.15	−25.7%	6.1%	−1.64%
$\Phi 273 \times 6 - 6 \times 48$	113.11	78.15	71.75	121.43	−30.9%	−36.6%	7.36%
$\Phi 273 \times 6 - 6 \times 72$	178.81	117.23	131.36	174.58	−34.4%	−26.5%	−2.36%
$\Phi 356 \times 8 - 8 \times 48$	173.15	86.98	84.76	171.19	−49.8%	−51.0%	−1.13%
$\Phi 356 \times 8 - 8 \times 120$	357.3	260.50	331.06	385.02	−27.1%	−7.3%	7.76%
Average	—	—	—	—	−33.5%	−18.3%	0.3%
Standard deviation	—	—	—	—	0.0830	0.2033	0.0518

0°, 90°, 180°, and −90° on the circular ring. This assumption raises two questions. First, the impact of the deformation on the remaining parts of the chord wall is not considered. Second, the variations in the curvature of each arc segment are not considered. Based on the comparison in Table 5 and Figure 18, notably, when the value of R was small, the T-shaped section reached yield; however, the remaining parts of the chord wall still had a certain bearing capacity. Therefore, the calculation result was rather small. When the value of R was high, the strength of the circular ring with a T-shaped section was greater. The total deformation of the chord wall reached 3% D because of the change in the curvature of the circular ring; however, the plastic hinge of the circular ring had not yet been fully formed. This led to higher calculation results. Therefore, a nonlinear regression analysis was employed to enhance the computational precision. These data, derived from tests and finite element calculations conducted for parameter analysis, were incorporated. Science $R \gg T/2 - \overline{y}$ and $D \gg T + 2\overline{y}$, make:

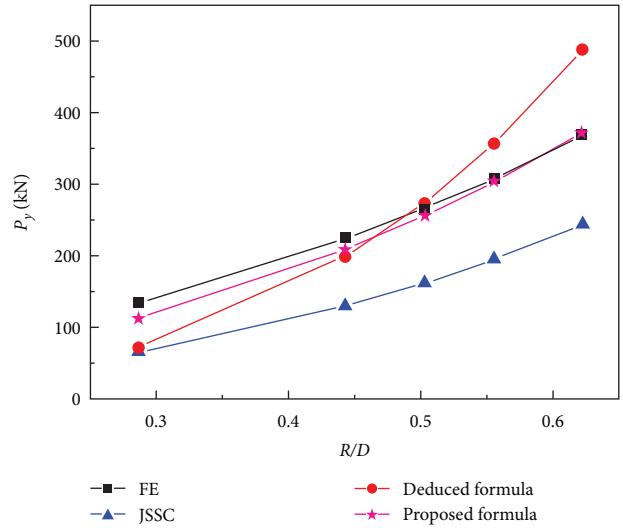

Figure 18: Comparison of the calculation results ($D = 194$ mm and $T = 6$ mm).

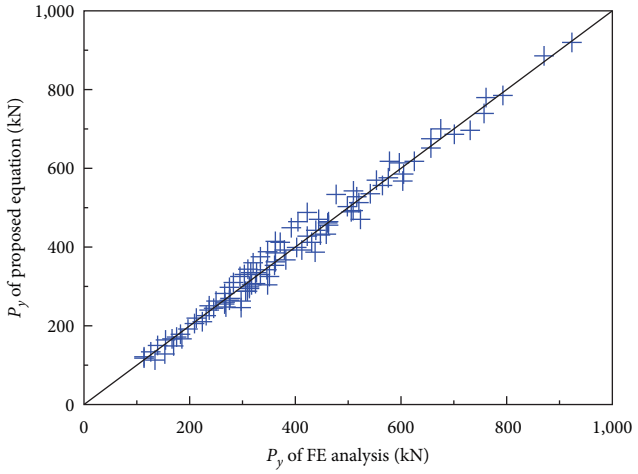

FIGURE 19: Comparison between the results from the proposed equation and FE results.

$$\frac{R + T/2 - \overline{y}}{D + T + \overline{y}} \approx \frac{R}{D}. \tag{16}$$

An optimal fit was achieved with a fitted correlation coefficient of 0.8480. The ultimate strengths of the X-joints were calculated as follows:

$$P_y = \left(BeT\sigma_y + Rt_r\sigma_{yr}\right)[0.4392(R/D)^3 - 2.1789(R/D)^2 + 2.5142(R/D) + 0.3464]. \tag{17}$$

6.2. Comparison with Existing Formulas. Table 5 lists the ultimate strength results obtained from the tests and existing formulae. In Table 5, "P_{y-1}" represents the calculation results of the derived formula, that is, Equation 15, and "P_{y-2}" represents the calculation results of the proposed formula, that is, Equation 17. As listed in Table 5, the results of the JSSC were considerably conservative, and the errors of the JSSC were approximately −33%. In comparison, the mean error of the proposed equation was 0.3%. Figure 18 illustrates the ultimate strength results obtained from the FE analysis and existing formulae. All the FE results were compared with the predictions from the proposed formula in Figure 19. The mean ratio of the formula calculation results to the FE results was 0.9937, and the standard deviation was 0.1168. The calculation results of the proposed formula (Equation 17) are closely aligned with the outcomes of the FE analyses, effectively reflecting the changes in the ultimate strength of the X-joints. Furthermore, the calculation process of the formula was recommended to be simplified compared to the design formula in Table 1. In summary, the proposed formula was stable and reliable, providing valuable insights into the design of ring-stiffened tube-gusset X-joints.

7. Conclusions

This study examined the mechanical behavior of X-type tube-gusset joints with ring plates. Based on the analysis results of the forces acting on the X-joints, we considered the forces acting on the X-joint as a superposition of the bending moment (M) and force (P). Through both experiments and FE analysis, the failure mode of the X-joints manifested as the deformation of the chord and warping of the ring plates, irrespective of the X-joint was subjected to a bending moment or force. Throughout the entire loading phase, the stress on the chord was notably high, only near the ring plate, whereas the stress at the other positions remained minimal. Therefore, we regarded the ring plate and the chord within the effective range of the ring plate as the primary bearing structure of the X-joint. The equivalent force at the ring plate position was used to determine the ultimate strength of the X-joints. In addition, a parameter analysis was performed using the verified simulation model, demonstrating a near-linear increase in the ultimate strength of the X-joint by increasing ratios R/D or t_r/T. By contrast, the changes caused by D/T were not significant. Finally, we devised a formula using a combination of theoretical derivations and regression analysis. These research findings provide a theoretical and experimental basis for the design of X-joints with ring plates.

Symbols

D: Chord external diameter
T: Chord thickness
R: Ring plate width
t_r: Ring plate thickness
B: Gusset plate length
t_g: Gusset plate thickness
H: Gusset plate width
F: Axial load of the braces
P_v: Force on the ring plate
P_y: Ultimate strength of the joint
Be: The effective range of the ring plate
σ_y, σ_{yr}: Yield strength of the chord, the ring plate
σ_{Br}: Tensile strength of the ring plate.

Data Availability

The (DATA TYPE) data used to support the findings of this study are included within the article.

Conflicts of Interest

All the authors declare that they have no known competing financial interests or personal relationships that could have appeared to influence the work reported in this paper.

Acknowledgments

Xiaolu Li reported that the financial support was provided by the Henan Provincial Department of Science and Technology (222102320114 and 222102320376).

References

[1] Y. Cai, T.-M. Chan, and B. Young, "Chord plastification in high strength steel circular hollow section X-joints: testing, modelling and strength predictions," *Engineering Structures*, vol. 243, Article ID 112692, 2021.

[2] L. Tian, J. Liu, C. Chen, L. Guo, M. Wang, and Z. Wang, "Experimental and numerical analysis of a novel tubular joint for transmission tower," *Journal of Constructional Steel Research*, vol. 164, Article ID 105780, 2020.

[3] H. Nassiraei and P. Rezadoost, "Local joint flexibility of tubular X-joints stiffened with external ring or external plates," *Marine Structures*, vol. 80, Article ID 103085, 2021.

[4] H. Nassiraei, A. Mojtahedi, M. A. Lotfollahi-Yaghin, and L. Zhu, "Capacity of tubular X-joints reinforced with collar plates under tensile brace loading at elevated temperatures," *Thin-Walled Structures*, vol. 142, pp. 426–443, 2019.

[5] L. Zhao, L. Zhu, H. Sun, L. Yang, and X. Chen, "Experimental and numerical investigation of axial tensile strength of CHS X-joints reinforced with external stiffening rings," *International Journal of Steel Structures*, vol. 20, no. 3, pp. 1003–1013, 2020.

[6] S. Saeko, "Experimental study on strength of tubular steel structures," *Japanese Society of Steel Construction*, vol. 10, pp. 37–68, 1974.

[7] X. L. Zhao, G. J. V. D. Vege, and I. I. W. New, "Static design recommendations for hollow section joints," 2008.

[8] J. Wardenier, Y. Kurobane, J. A. Packer, D. Dutta, and N. Yeomans, "Design guide for circular hollow section (CHS) joints under predominantly static loading," 1991.

[9] H. D. Lee, J. M. Lee, S. H. Lee, and K. J. Shin, "Investigation of the tube-gusset connection in 600 MPA circular hollow section," *Procedia Engineering*, vol. 14, pp. 2124–2132, 2011.

[10] American Institute of Steel Construction, "Steel construction manual," 2011.

[11] H. Nassiraei and P. Rezadoost, "Static capacity of tubular X-joints reinforced with fiber reinforced polymer subjected to compressive load," *Engineering Structures*, vol. 236, Article ID 112041, 2021.

[12] H. Nassiraei and P. Rezadoost, "Probabilistic analysis of the ultimate strength of tubular X-joints stiffened with outer ring at ambient and elevated temperatures," *Ocean Engineering*, vol. 248, Article ID 110744, 2022.

[13] H. Nassiraei, "Probability distribution functions for the ultimate strength of X-joints with collar plates in compressive load at room and fire conditions," *Structures*, vol. 59, Article ID 105703, 2024.

[14] H. Nassiraei, "Local joint flexibility of CHS X-joints reinforced with collar plates in jacket structures subjected to axial load," *Applied Ocean Research*, vol. 93, Article ID 101961, 2019.

[15] H. Nassiraei, L. Zhu, M. A. Lotfollahi-Yaghin, and H. Ahmadi, "Static capacity of tubular X-joints reinforced with collar plate subjected to brace compression," *Thin-Walled Structures*, vol. 119, pp. 256–265, 2017.

[16] P. Rezadoost and H. Nassiraei, "Identification of the most suitable probability distributions for ultimate strength of FRP-strengthened X-shaped tubular joints under axial loads," *Ocean Engineering*, vol. 290, Article ID 116292, 2023.

[17] Japanese Society of Steel Construction, "Electricity transmitting steel tubular tower manufacture norm," 1995.

[18] Northwest Electric Power Design Institute Co. Ltd, "Experimental study report to tube-gusset joints stiffened by ring plate in steel tube tower," Xi'an, (In Chinese), 2016.

[19] F. Li, H.-Z. Deng, and X.-Y. Hu, "Resistance of gusset-tube DK-joints stiffened by 1/2 annular plates in transmission towers," *Journal of Constructional Steel Research*, vol. 159, pp. 560–573, 2019.

[20] F. Li, H.-Z. Deng, and X.-Y. Hu, "Experimental and numerical investigation into ultimate capacity of longitudinal plate-to-circular hollow section K- and DK-joints in transmission towers," *Thin-Walled Structures*, vol. 143, Article ID 106240, 2019.

[21] X. Li, L. Zhang, X. Xue, X. Wang, and H. Wang, "Prediction on ultimate strength of tube-gusset KT-joints stiffened by 1/4 ring plates through experimental and numerical study," *Thin Walled Structures*, vol. 123, pp. 409–419, 2018.

[22] X. Li, X. Xue, L. Zhang, X. Wang, and H. Wang, "Experiment and finite element analysis on the ultimate strength of ring-stiffened tube-gusset joints," *International Journal of Steel Structures*, vol. 19, no. 5, pp. 1534–1542, 2019.

[23] S. Qu, X. Wu, and Q. Sun, "Experimental study and theoretical analysis on the ultimate strength of high-strength-steel tubular K-Joints," *Thin-Walled Structures*, vol. 123, pp. 244–254, 2018.

[24] S. Qu, J. Yuan, Q. Zhang, B. Zhang, and Q. Sun, "Calculating the ultimate strength of a tube-gusset KT joint with 1/4 ring stiffener plates," *Thin-Walled Structures*, vol. 185, Article ID 110631, 2023.

[25] S. Qu, J. Yuan, B. Zhang, and Q. Sun, "Calculating the nonlinear stiffness and ultimate strength of tube-gusset plate joints in circular hollow sections," *International Journal of Civil Engineering*, vol. 22, no. 4, pp. 549–580, 2024.

[26] S. Qu, Q. Li, Y. Wang, J. Yuan, and Q. Sun, "Failure pattern and load distribution mechanism of stiffeners in the tube-gusset plate connection: testing, numerical modelling and theoretical analysis," *Structures*, vol. 36, pp. 951–978, 2022.

[27] S. Qu, S. Wei, J. Yuan, and Q. Sun, "Tension and compression stiffness of ring stiffener in tube-gusset plate connections," *Thin-Walled Structures*, vol. 166, Article ID 108067, 2021.

[28] S. Qu, J. Yuan, B. Zhang, and Q. Sun, "Ultimate strength of multiplanar KT-type tube-gusset plate joint with half-ring stiffener plates," *Journal of Constructional Steel Research*, vol. 203, Article ID 107834, 2023.

[29] Q. Sun, S. Qu, and X. Wu, "Ultimate load capacity analysis of Q690 high-strength steel KK-type tube-gusset plate connections," *Journal of Structural Engineering*, vol. 145, no. 8, Article ID 04019074, 2019.

[30] W. Sitong, Z. Jinghua, Z. Chao, W. Xueming, and S. Qing, "Study on the analytical model for load distribution of multiple-ring-stiffened tube-gusset joints considering ring stiffness," *Structures*, vol. 51, pp. 1852–1868, 2023.

[31] Y. Chen, Z. Hu, Y. Guo et al., "Ultimate bearing capacity of CHS X-joints stiffened with external ring stiffeners and gusset plates subjected to brace compression," *Engineering Structures*, vol. 181, pp. 76–88, 2019.

[32] G. J. V. D. Vegte and Rny Makino, "Further research on chord length and boundary conditions of chs T- and X-joints," *Advanced Steel Construction*, vol. 6, pp. 879–890, 2010.

[33] Y.-B. Shao, S.-T. Lie, S.-P. Chiew, and Y.-Q. Cai, "Hysteretic performance of circular hollow section tubular joints with collar-plate reinforcement," *Journal of Constructional Steel Research*, vol. 67, no. 12, pp. 1936–1947, 2011.

[34] X. Lan and Y. Huang, "Structural design of cold-formed stainless steel tubular X- and T-joints at elevated temperatures," *Thin-Walled Structures*, vol. 108, pp. 270–279, 2016.

[35] H. Ahmadi, A. Yeganeh, A. H. Mohammadi, and E. Zavvar, "Probabilistic analysis of stress concentration factors in tubular KT-joints reinforced with internal ring stiffeners under in-plane bending loads," *Thin-Walled Structures*, vol. 99, pp. 58–75, 2016.